Microstructure and Mechanical Properties of Copper–steel Laminated and Sandwich Joints Prepared by Electron Beam Welding

Song Debin, Wang Ting, Jiang Siyuan, and Zhang Liang

Laminated and sandwich joints composed of copper and 304 stainless steel with different stacking sequences were prepared by electron beam welding. The analysis of microstructures, element distribution and mechanical properties of the joints were carried out. Joints under all parameters were well formed without defects such as pores and cracks. The microstructures of the welds were mainly composed of (Cu, Fe) solid solution [(Cu, Fe)ss]. It was also found that the shear strength of the joint and the content of α-phase at the interface had a linear relationship. For laminated joints, the shear strength of steel/copper joint was increased by 12.7% compared with copper/steel joint, and the shear strength value reached 420 MPa. The scanning electron beam could refine microstructures and increase the weld width and improve the mechanical properties of the joints significantly. The tensile strength of the sandwich joint with steel as the intermediate layer was increased by 17.4% compared with the joint with copper as the intermediate layer.

1. Introduction

Copper alloys have been widely used in aerospace, food machinery and metallurgy due to their excellent thermal conductivity, electrical conductivity and good ductility (Ref 1). Stainless steel has been widely used because of its high strength and lower cost (Ref 2), which can effectively improve mechanical strength (Ref 3). Therefore, copper–steel laminated and sandwich structures [such as cooling staves (Ref 4) and corrosion-resistant structural parts (Ref 5)] can meet various performance requirements under the condition of saving precious metals and reducing costs (Ref 6, 7).

However, due to the large difference in melting point, coefficient of linear expansion, thermal conductivity, and mechanical properties between copper and stainless steel, welding two materials becomes difficult (Ref 8-10). Sahin et al. (Ref 11) successfully used friction welding to obtain a joint with a strength of 75 MPa. Satpathy et al. (Ref 12) studied the effect of welding parameters on ultrasonic spot welded copper–steel joints. It was found that under different welding parameters, Cu on the sonotrode side had a higher bonding strength

than AISI 304 stainless steel. At present, copper/steel composite plates are mainly prepared by explosive welding (Ref 13-15). However, the thickness of the plates has a great influence on the performance of the composite plates made by explosion welding (Ref 16). It is difficult to connect the plates with large thickness by explosive welding. Electron beam welding (EBW) has the advantages of high processing accuracy, high efficiency, and high depth-to-width ratio (Ref 17-19). It has obvious advantages when welding copper/stainless steel dissimilar materials (Ref 20). However, there has been no report on the preparation of copper/steel composite plates by EBW so far.

The purpose of this study is to analyze the microstructure and mechanical properties of EBW joints of laminated and sandwich structures with different overlapping sequences. The effect of the scanning electron beam on the joints was also discussed.

2. Experimental Procedure

2.1 Materials and Experimental Methods

In this experiment, copper (T2) and 304 stainless steel plates with a size of 100 mm × 50 mm × 2 mm were selected as base metals (BM). The samples were polished with sandpaper to remove the surface oxide film before welding and then wiped the sample with acetone to remove surface grease.

The BMs cleaned before welding were clamped on the welding fixture in a certain order, and the joints were in the form of overlap (Fig. 1). During the welding process, the acceleration voltage of the electron gun (70 kV) and the focusing current (585 mA) remained unchanged, and the beam was focused on the sample surface. For laminated joints, welding was performed from the steel side or the copper side, and two sets of parameters were selected for each direction. The sandwich joints used copper as the middle sandwich or steel as the middle sandwich. Table 1 shows the welding parameters.

Song Debin, Wang Ting, and **Jiang Siyuan**, State Key Laboratory of Advanced Welding and Joining, Harbin Institute of Technology at Weihai, Weihai 264209, People's Republic of China; and Shandong Provincial Key Laboratory of Special Welding Technology, Harbin Institute of Technology at Weihai, Weihai 264209, People's Republic of China; **Zhang Liang**, Shenzhen Polytechnic, Institute of Intelligent Manufacturing Technology, Shenzhen 518055, People's Republic of China. Contact e-mail: fgwangting@163.com.
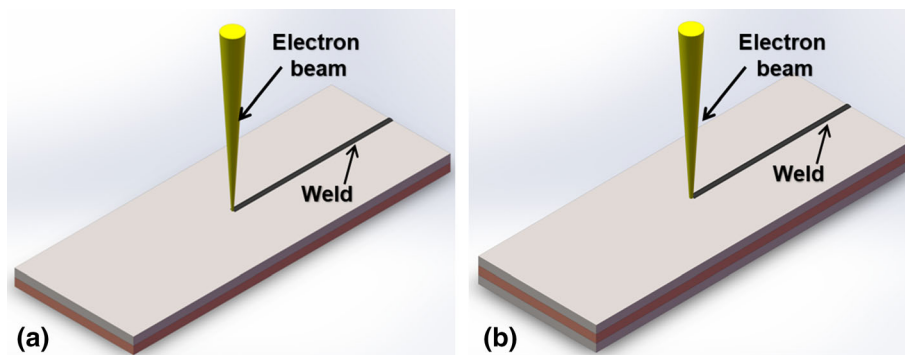
2.2 Characterization of the Joints

After welding, wire-cut electric discharge machining was used to intercept the metallographic samples along the vertical welding direction in the stable area of joints. Afterward, the inlaid samples were polished by sandpaper from 80# to 5000# step by step and then mechanically polished by diamond polish. The observation surface was chemically etched in the corrosive agent [FeCl₃ (3 g) + HCl (2 mL) + ethanol (96 mL)] for about 5 s. The microstructure of the joints was observed by OLYMPUS optical microscope (OM) and MERLIN Compact scanning electron microscopy (SEM). Distributions of chemical elements in the fusion zone were analyzed by the energy-dispersive spectroscopy (EDS) in the spot and line modes.

Tensile tests were carried out using an Instron 5967 universal testing machine at room temperature. The samples were cut along the vertical weld line, and the size of the sample is shown in Fig. 2(a). Tensile rate was 0.5 mm/min. Three samples were tested for each welding and average values are reported. In order to ensure that the direction of the tensile force of the samples was perpendicular to the welds, pads with the same thickness as BMs were placed on both sides of the samples (seen in Fig. 2b and c). Microhardness of the joints was measured by a HV-1000T standard microhardness tester. The indentation distance was 0.05 mm, the load was 0.98 N, and the holding time was 10 s.

Table 1 Welding parameters used in the experiments

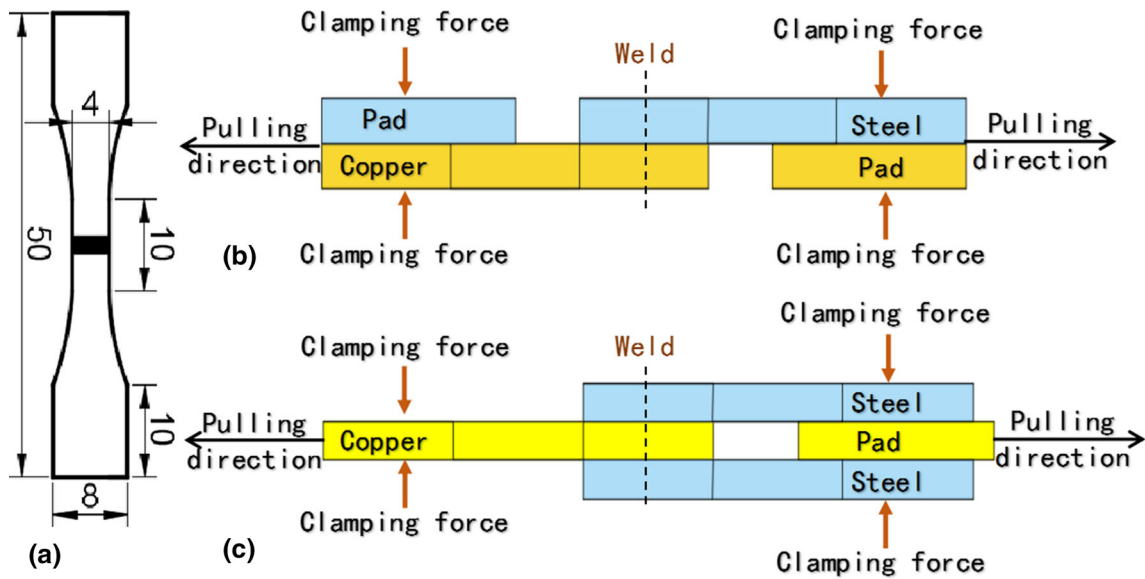| Joint (No.)	Structure form	Beam current, mA	Welding speed, mm/min	Beam scanning
1#	Copper/steel	19	600	No
2#		19	600	Yes
3#	Steel/copper	19	600	No
4#		19	600	Yes
5#	Copper/steel/copper	32	600	No
6#		32	600	Yes
7#	Steel/copper/steel	25	600	No
8#		28	600	Yes

3. Results and Discussion

3.1 Joint Microstructure Analysis

3.1.1 Microstructure Analysis. The cross-sectional morphologies of the EBW joints are shown in Fig. 3. Low heat input prevented the pores and cracks reported in Ref 21 from forming in the welds. The fusion borders of the weld seam near the steel side were clear. However, due to the strong heat dissipation capacity of copper, the fusion lines near the copper side were not obvious. The large heat dissipation capacity was also the main factor that leaded to the decrease in the width of the weld on the copper side. The different stacking order had great influence on the microstructure of the weld. For laminated joints, when welding from the steel side, the uniformly distributed Cu_{ss} and Fe_{ss} in the middle of the weld of Joint 1 were replaced by Cu_{ss} and Fe_{ss} alternately distributed in an arc shape.

Microstructures of the different zones of the joints can be seen in Fig. 4, and the characteristic regions of the weld were analyzed by EDS (Fig. 5). According to the binary Cu-Fe equilibrium diagram (Ref 22), as shown in Fig. 6, the welds were mainly composed of two phases, one was α-phase which was rich in Fe, Cr and Mn. The other was ε-phase which was rich in Cu (Ref 23, 24). Due to the high cooling rate, a large number of isolated α-phases were found in the weld shown in Fig. 4(a). In Fig. 4(b), the phenomenon of the steel flowing upward along the sidewall under the action of buoyancy can be seen on both sides of the weld at the interface. During the solidification process of the weld, the low melting point and solid solubility of copper in austenite were the reasons for the dendritic distribution of copper at the grain boundaries of α-phase in Fig. 4(c). The same conclusion was also obtained by Guo et al. (Ref 22). Near the center of the weld, the granular α-phases can be found in the copper matrix, as shown in Fig. 4(e). Whether it was a laminated joint or a sandwich joint, some vortices were formed at the interfaces between the copper BMs and the weld due to the lack of heat inputs, and there were still some small granular α-phases in the vortices.

3.1.2 Formation Mechanism of Joint Cross Section. The formation mechanism of the microstructures is shown in Fig. 7. It can be seen from Fig. 7(a) that for copper/steel joint, the upper part of the weld seam was evenly mixed during welding. When cooling, ε-phases were crystallized from the liquid phase. When the temperature continued to decrease, the α-phases were precipitated from the solid phase. In the

Fig. 1 Schematic diagrams of the welding experiments of (a) laminated and (b) sandwich structures

Fig. 2 Schematic diagram of mechanical property tests: (a) dimensions of tensile sample (b) schematic diagram of the tensile test for laminated joints (c) schematic diagram of the tensile test for sandwich joints
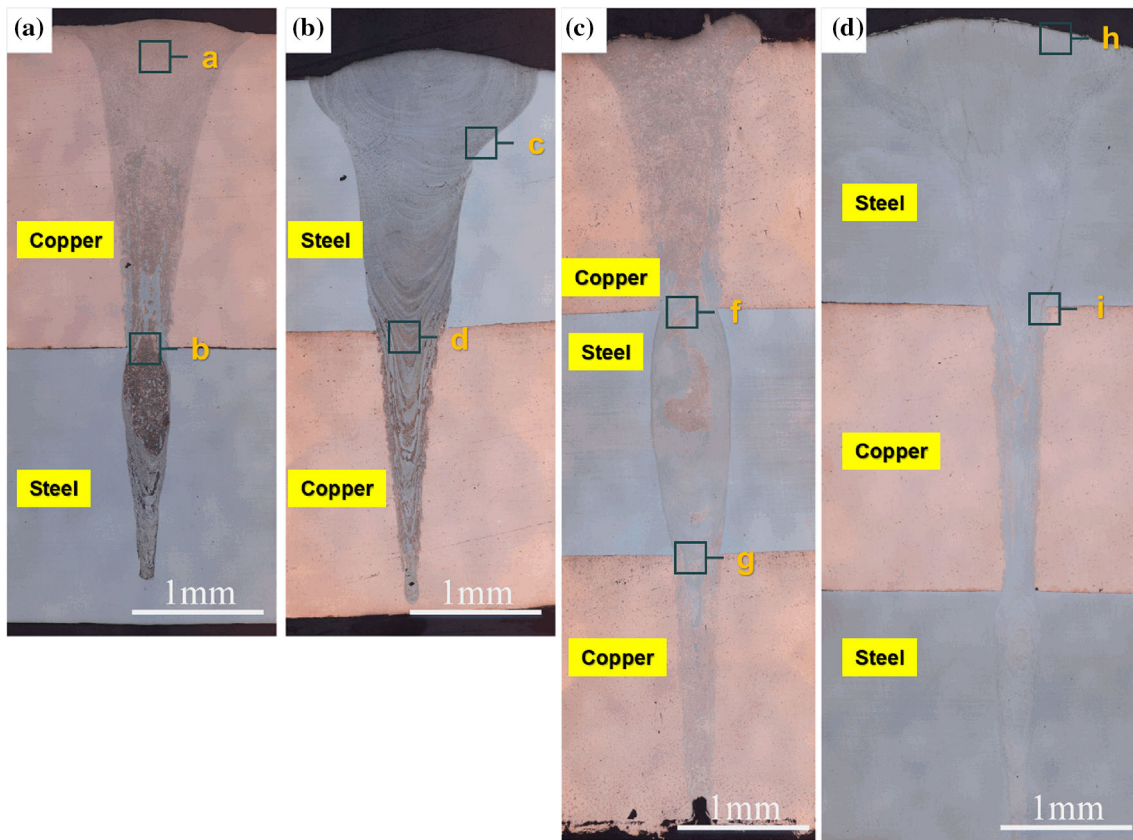

Fig. 3 Macrostructures of cross sections of (a) electron beam welded copper/steel joint, (b) electron beam welded steel/copper joint, (c) electron beam welded copper/steel/copper joint and (d) electron beam welded steel/copper/steel joint

middle of the weld, due to the extremely short residence time at the high-temperature stage during welding, the molten copper and steel had no time to mix evenly, the under-mixed molten steel flowed upward under the effect of buoyancy. The formation mechanism of steel/copper joint is shown in Fig. 7(b). The content of α-phase in the weld increased gradually with the temperature decreases, and finally, ε-phase precipitated at the grain boundaries of α-phase. At the interface of the weld seam, the thermal conductivity of copper was much higher than that of steel. Therefore, under-mixed copper and
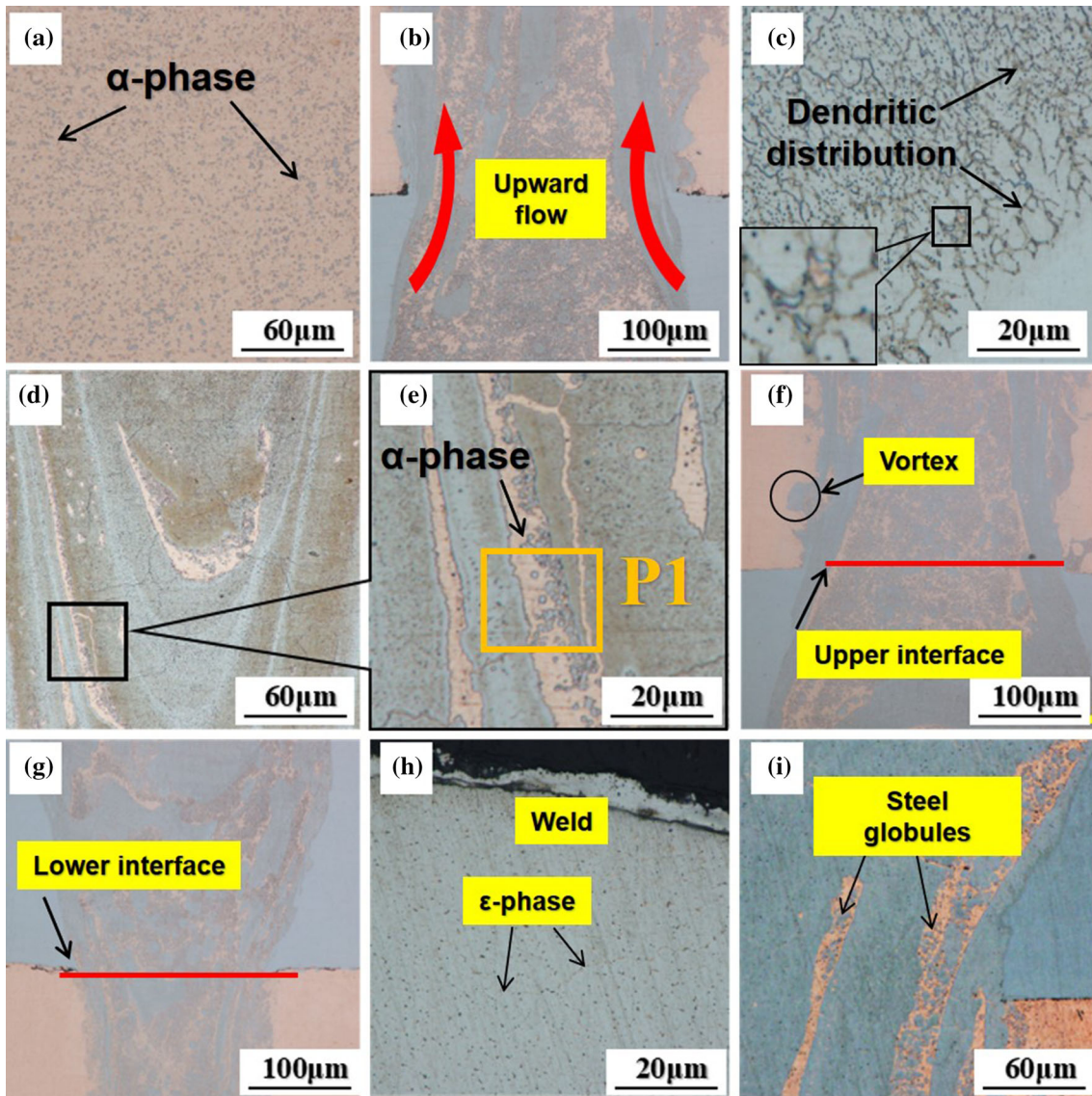
Fig. 4 Microstructures of the different zones in the joints: (a) and (b) electron beam welded copper/steel joint, (c) and (d) electron beam welded steel/copper joint, (f) and (g) electron beam welded copper/steel/copper joint, (h) and (i) electron beam welded steel/copper/steel joint

Point	Fe/%	Cu/%
A	82.59	17.41
B	11.26	88.74
C	18.06	81.94
D	73.59	26.41
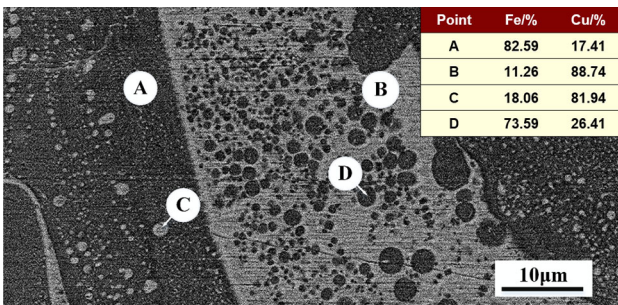
Fig. 5 EDS test areas and test results

steel would grow in the direction of faster heat dissipation.

3.1.3 Element Distribution Analysis. Figure 8 shows the scan results of laminated joints. The copper content of the joints welded from the copper side at the upper of the weld was about 83.8%. At the interface of the weld, due to the upward flow of the steel along the inside of the weld, the steel content increased significantly. For steel/copper joints, in the middle and lower part of the weld, an alternating strip of copper and steel was presented, which made the composition of the weld fluctuate greatly. The trends of chromium and nickel content in the weld were the same as that of iron. The reason was probably that the time was too short to mix the steel and copper melt effectively (Ref 21).

3.2 Mechanical Properties

3.2.1 Shear Strength and Fracture Analysis. Figure 9 shows the results of the tensile tests of laminated joints. The fractures of all joints in this article are broken along the weld seam. The different overlapping sequences changed the composition of phases at the interface, which was the reason for the difference in the tensile strength. Due to the large amount of melting of Cu BMs, the strength of copper/steel joint was reduced due to the increase in ε-phase ratio at the interface. Kar
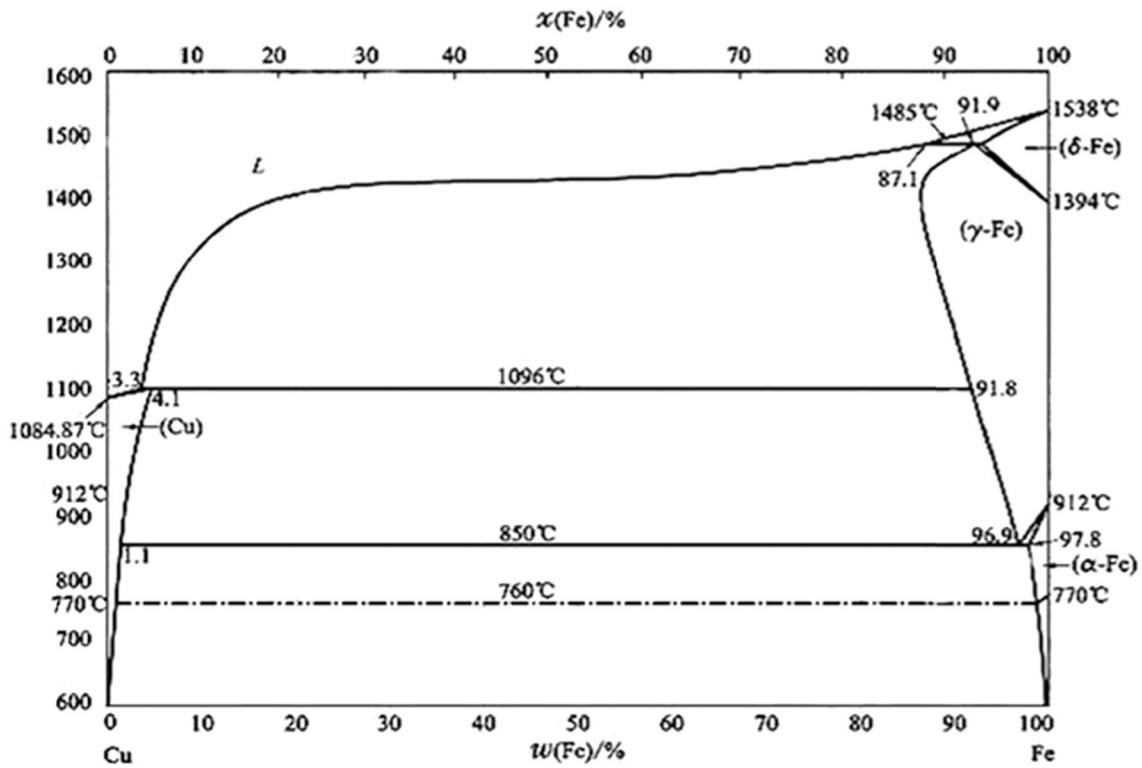
Fig. 6 Binary Cu-Fe equilibrium diagram [22]

et al. (Ref 25) reported that the beam oscillation made copper and steel better mixed. Meng et al. (Ref 26) believed that evenly distributed α-phases in the copper matrix could strengthen the weld. At the same time, the circular oscillating scanning allowed copper atoms to melt into the α-phase better and thus increased the ratio of α-phase at the interface. Yang et al. (Ref 27) also found that the circular oscillating scanning could achieve dendrite refinement. According to the Hall–Petch formula (Ref 28), the refinement of grains can effectively improve the joint strength. Therefore, the strength of the joints had increased to varying degrees under the action of the beam oscillation.

For sandwich joints, when a fracture occurred on one side of the weld, the tensile test was stopped, and the tensile test results are shown in Table 2.

As can be seen from Table 2, when steel was used as the intermediate interlayer, the EBW joints could withstand the tension more strongly. The fracture was produced at the lower interface of the weld because the width of the weld at the lower interface was narrower than the upper interface, which made it the weakest link in the joints.

Fracture surface morphologies of the joints are shown in Fig. 10. The fracture surfaces of steel/copper joint shown in Fig. 10(a) and (b) were lamellar, and the beginnings of the slices were covered with dimples of different sizes. The existence of dimples proved that the fracture conformed to the basic characteristics of ductile fracture. Figure 10(c) and (d) is fracture surfaces of copper/steel joint. The fracture surfaces were flush, and a large number of dimples were generated on the surface. This phenomenon was attributed to the uniform distribution of the components at the joint interfaces, so the concentration distribution of stress was uniform during the stretching process. The EDS results of the fracture areas have

shown that the location of the dimple and lamellar tissue in the fracture area may be generated in the α-phase areas or the ε-phase areas.

3.2.2 Microhardness. Figure 11 shows the Vickers microhardness test results of EBW joints. Guo et al. (Ref 22) believed that an increase in the proportion of steel in welding pool would result in an increase in the value of hardness. The variation trend of hardness and α-phase content in the figure also proved this. Copper/steel joints had a characteristic of a sharp decrease in the direction of the weld due to the ε-phase in the joints. Figure 11(b) shows the hardness distribution along the direction of the weld when welding from the copper side. The hardness of joints as a whole presented a gradually increasing trend from top to bottom as shown in Fig. 11(a). At the lower end of the weld, the hardness gradually tended to the BM.

3.3 Effect of Microstructure on Mechanical Properties

The composition of the phases at the interface had a greater influence on the shear strength of the joints (Ref 26). The mechanical properties of the joints would enhance as the proportion of copper at the interface decreases (Ref 29). In optical images, the α-phase and ε-phase can be distinguished by different colors. Therefore, Image-pro plus (IPP) software was used to measure the proportion of the α-phase at the interface of joints. The measured proportion of α-phases and ε-phases and the actual shear strength are listed in Table 3. Least square linear fitting was used to establish the relationship between the steel content at the interface and the shear strength of the joint, and the fit result is shown in Fig. 12(b). The linear relationship is $Y = 237.36X + 195.51$ (Y is the shear strength, and Z is the steel content at the interface). Therefore, the welding param-
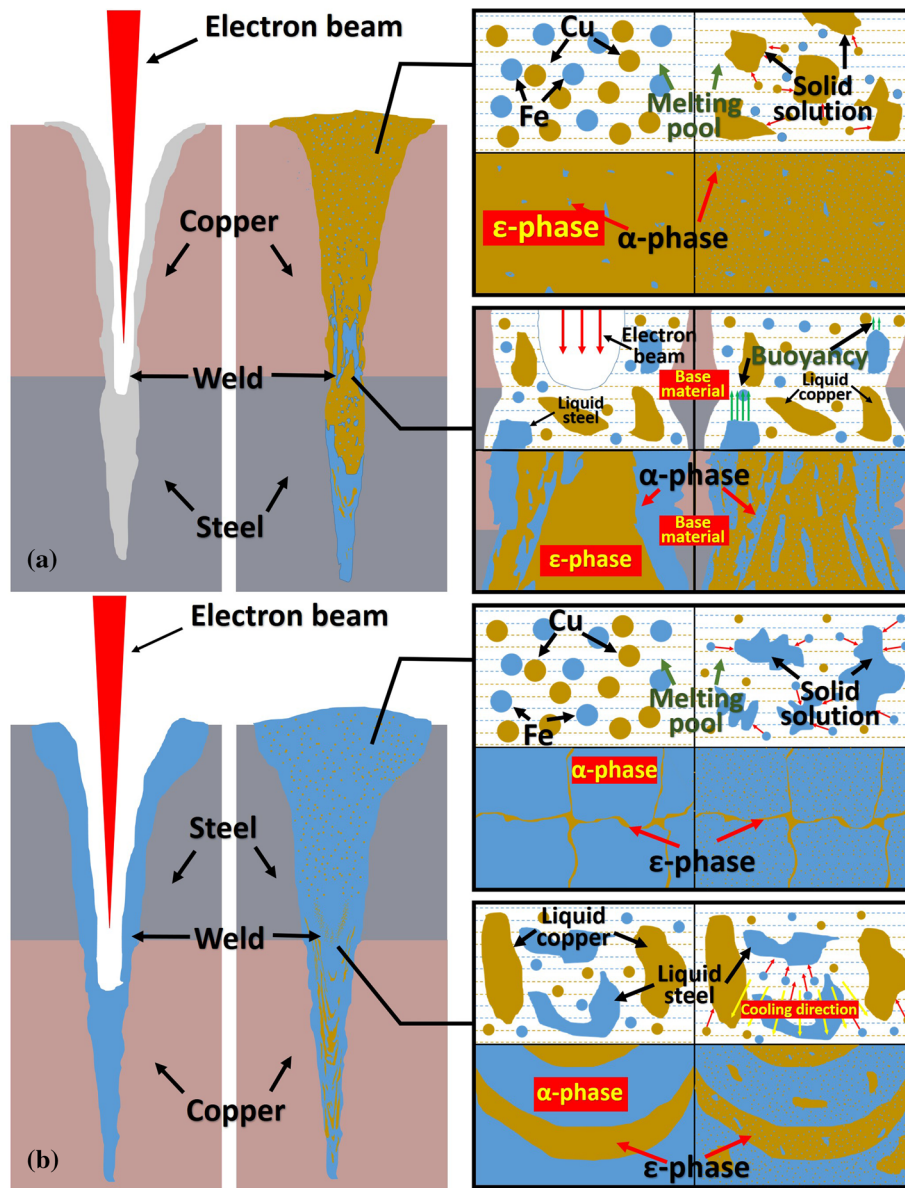
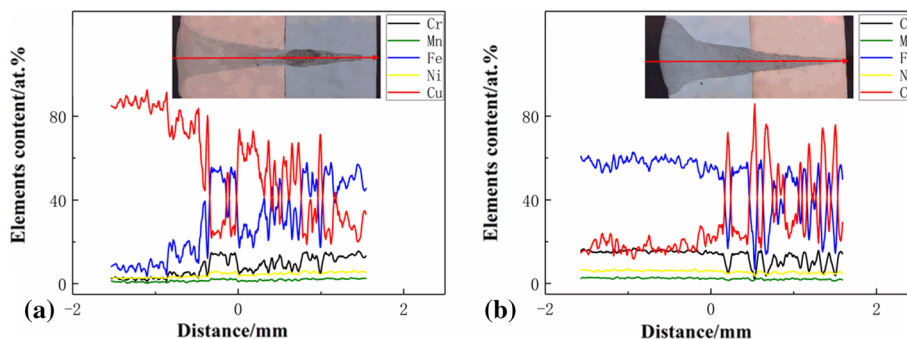**Fig. 7** The formation mechanisms of the microstructures of (a) copper/steel and (b) steel/copper joints

Fig. 8 Element distributions of electron beam welded laminated structure joints

eters could be adjusted to increase the content of α-phase at the interface to obtain the highest tensile strength.

The above-mentioned linear fitting formula was used to predict the shear strength of the upper and lower interfaces of the sandwich joint. The anticipated values of the shear strength are listed in Table 4. It can be seen from the predicted results that when steel is an intermediate sandwich, the scanning electron beam will reduce the shear strength of the joint. When

copper is used as the intermediate sandwich, the shear strength of the upper and lower interfaces will be higher than that of steel as the intermediate sandwich. However, in the actual tensile experiments, the bearing capacity of the tensile sample when the steel was used as the interlayer was higher than that of the copper as the sandwich. The analysis showed that although steel was used as the intermediate layer, the content of the steel at the upper and lower interfaces of the joint was lower than that when copper was used as the intermediate layer. However, the width of the upper and lower interfaces of the weld was basically the same. When copper was used as the middle layers, the weld width was significantly reduced by a large amount of heat loss. Moreover, there was still copper flowing down from the intermediate plates, making the lower interface of the weld seam a weak zone of the weld seam, which severely reduced the ability of the steel/copper/steel joint to withstand tension.

4. Conclusions

All joints were a mixture of two non-equilibrium phases, one rich in Cu and one rich in Fe, Cr and Ni. This was mainly due to the higher cooling rate and the lower solubility of copper and iron in the solid state.

For laminated joints, the shear strength of steel/copper joint was higher than that of copper/steel joint. Scanning electron beam welding can significantly increase the strength of copper/steel joint. The sandwich joints with steel as the middle layer can withstand higher tensile forces.

The hardness of the steel/copper joint almost unchanged from top to bottom, but the hardness of copper/steel joint gradually increased from top to bottom. At the end of the weld, the hardness was close to the BMs.

There was a linear relationship between the content of α-phase at the weld interface and the shear strength of the joint.
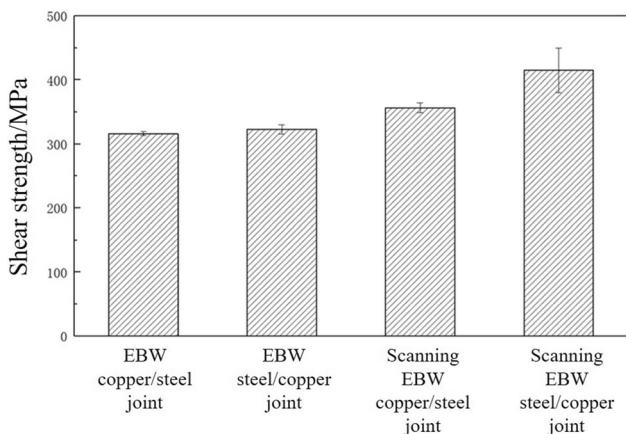
Fig. 9 Tensile shearing strengths of different joints

Table 2 Tensile test results

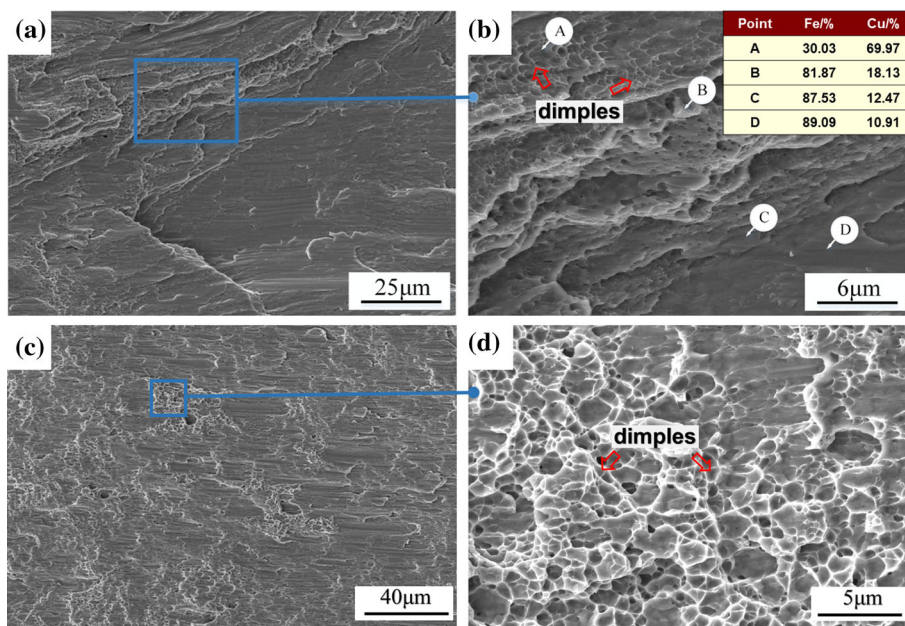| Structure form	Tensile load, N	Upper interface width, mm	Lower interface width, mm
Copper/steel/copper	1387	0.62	0.50
Steel/copper/steel	1181	0.60	0.31

Fig. 10 Fracture surface morphologies of (a-b) copper/steel joint and (c-d) steel/copper joint
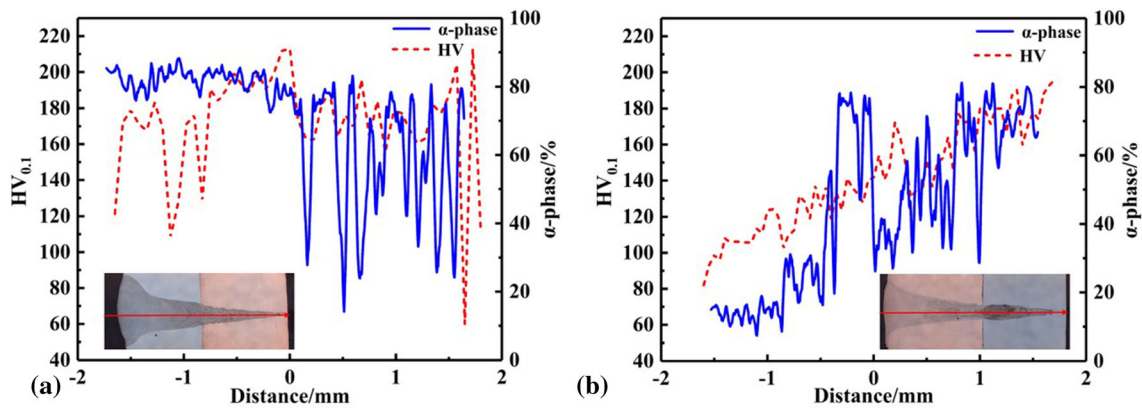
Fig. 11 Microhardness test results of (a) steel/copper and (b) copper/steel joints

Table 3 Copper–steel ratio measurement results at the interface of laminated joints

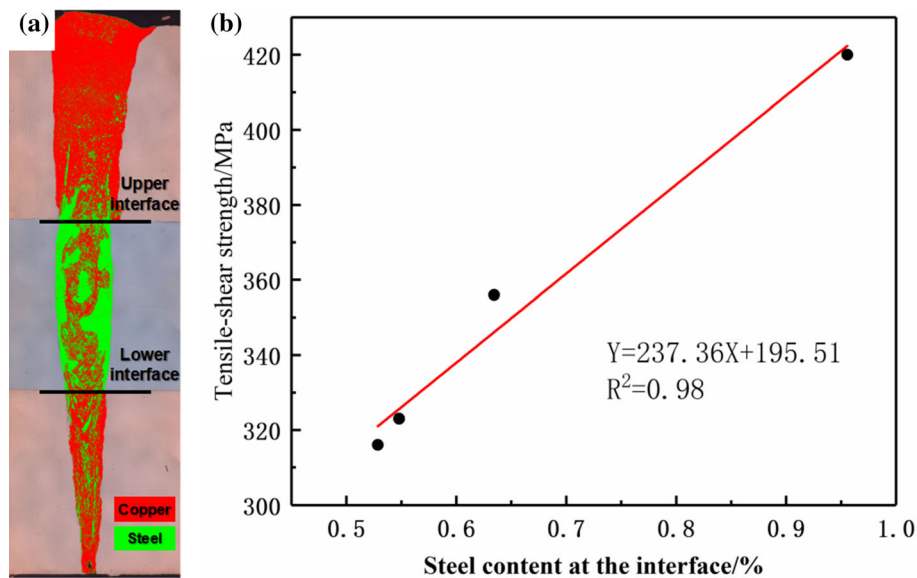| Structure form	Beam scanning	Fe, %	Cu, %	Shear strength, MPa
Copper/steel	No	52.86	47.14	316
	Yes	54.80	45.20	323
Steel/copper	No	63.44	36.56	356
	Yes	95.56	4.44	420

Fig. 12 (a) IPP software processing diagram and (b) Linear fitting results of steel content and shear strength at the joint interface

Table 4 Predicted values of shear strength

Structure form	Beam scanning	Upper interface steel content, %	Upper interface strength, MPa	Lower interface steel content, %	Lower interface strength, MPa
Copper/ steel/copper	No	86.96	401.94	71.12	364.32
	Yes	69.68	360.92	49.32	312.56
Steel/copper/ steel	No	92.09	414.10	99.24	431.07
	Yes	98.26	428.74	92.05	414.02

The linear equation is $Y = 237.36X + 195.51$ (Y is the shear strength, and Z is the steel content at the interface).

Acknowledgments

Conflict of interest

The authors declare that they have no known competing financial interests or personal relationships that could have appeared to influence the work reported in this paper.

References

1. S.G. Shiri, M. Nazarzadeh, M. Sharifitabar, and M.S. Afarani, Gas Tungsten Arc Welding of CP-Copper to 304 Stainless Steel Using Different Filler Materials, *Trans. Nonferrous Metals Soc. China*, 2012, **22**, p 2937–2942

2. B. Zhang, T. Wang, X. Duan, G. Chen, and J. Feng, Temperature and Stress Fields in Electron Beam Welded Ti-15-3 Alloy to 304 Stainless Steel Joint with Copper Interlayer Sheet, *Trans. Nonferrous Metals Soc. China*, 2012, **22**, p 398–403

3. J. Yang, Y. Li, F. Wang, Z. Zang, and S. Li, New Application of Stainless Steel, *J. Iron Steel Res. Int.*, 2006, **13**, p 62–66

4. H. Zhang, K.X. Jiao, J.L. Zhang, and J. Liu, Experimental and Numerical Investigations of Interface Characteristics of Copper/Steel Composite Prepared by Explosive Welding, *Mater. Des.*, 2018, **154**, p 140–152

5. M. Weigl and M. Schmidt, Influence of the Feed Rate and the Lateral Beam Displacement on the Joining Quality of Laser-Welded Copper-Stainless Steel Connections, *Phys. Procedia*, 2010, **5**, p 53–59

6. S. Chen, J. Huang, J. Xia, X. Zhao, and S. Lin, Influence of Processing Parameters on the Characteristics of Stainless Steel/Copper Laser Welding, *J. Mater. Process. Technol.*, 2015, **222**, p 43–51

7. S. Patra, K.S. Arora, M. Shome, and S. Bysakh, Interface Characteristics and Performance of Magnetic Pulse Welded Copper-Steel Tubes, *J. Mater. Process. Technol.*, 2017, **245**, p 278–286

8. A. Mannucci, I. Tomashchuk, V. Vignal, P. Sallamand, and M. Duband, Parametric study of Laser Welding of Copper to Austenitic Stainless Steel, *Procedia CIRP*, 2018, **74**, p 450–455

9. B. Zhang, J. Zhao, X. Li, and J. Feng, Electron Beam Welding of 304 Stainless Steel to QCr0.8 Copper Alloy with Copper Filler Wire, *Trans. Nonferrous Metals Soc. China*, 2014, **24**, p 4059–4066

10. J. Li, Y. Cai, F. Yan, C. Wang, Z. Zhu, and C. Hu, Porosity and Liquation Cracking of Dissimilar Nd:YAG Laser Welding of SUS304 Stainless Steel to T2 Copper, *Opt. Laser Technol.*, 2020, **122**, p 105881

11. M. Sahin, E. Çıl, and C. Misirli, Characterization of Properties in Friction Welded Stainless Steel and Copper Materials, *J. Mater. Eng. Perform.*, 2013, **22**, p 840–847

12. M.P. Satpathy, A. Kumar, and S.K. Sahoo, Effect of Brass Interlayer Sheet on Microstructure and Joint Performance of Ultrasonic Spot-Welded Copper-Steel Joints, *J. Mater. Eng. Perform.*, 2017, **26**, p 3254–3262

13. S.V. Gladkovsky, S.V. Kuteneva, and S.N. Sergeev, Microstructure and Mechanical Properties of Sandwich Copper/Steel Composites Produced by Explosive Welding, *Mater. Charact.*, 2019, **154**, p 294–303

14. A. Durgutlu, B. Gülenç, and F. Findik, Examination of Copper/Stainless Steel Joints Formed by Explosive Welding, *Mater. Des.*, 2005, **26**, p 497–507

15. M.H. Bina, F. Dehghani, and M. Salimi, Effect of Heat Treatment on Bonding Interface in Explosive Welded Copper/Stainless Steel, *Mater. Des.*, 2013, **45**, p 504–509

16. A. Durgutlu, H. Okuyucu, and B. Gulenc, Investigation of Effect of the Stand-Off Distance on Interface Characteristics of Explosively Welded Copper and Stainless Steel, *Mater. Des.*, 2008, **29**, p 1480–1484

17. S. Wang and X. Wu, Investigation on the Microstructure and Mechanical Properties of Ti–6Al–4V Alloy Joints with Electron Beam Welding, *Mater. Des. (1980-2015)*, 2012, **36**, p 663–670

18. K. Han, H. Wang, L. Shen, and B. Zhang, Analysis of Cracks in the Electron Beam Welded Joint of K465 Nickel-Base Superalloy, *Vacuum*, 2018, **157**, p 21–30

19. L. Zhao, S. Wang, Y. Jin et al., Microstructural Characterization and Mechanical Performance of Al–Cu–Li Alloy Electron Beam Welded Joint, *Aerosp. Sci. Technol.*, 2018, **82–83**, p 61–69

20. M.S. Węglowski, S. Błacha, and A. Phillips, Electron Beam Welding—Techniques and Trends—Review, *Vacuum*, 2016, **130**, p 72–92

21. I. Magnabosco, P. Ferro, F. Bonollo, and L. Arnberg, An Investigation of Fusion Zone Microstructures in Electron Beam Welding of Copper–Stainless Steel, *Mater. Sci. Eng. A*, 2006, **424**, p 163–173

22. S. Guo, Q. Zhou, J. Kong, Y. Peng, Y. Xiang, T. Luo, K. Wang, and J. Zhu, Effect of Beam Offset on the Characteristics of Copper/304 Stainless Steel Electron Beam Welding, *Vacuum*, 2016, **128**, p 205–212

23. Z. Cheng, H. Liu, J. Huang, Z. Ye, J. Yang, and S. Chen, MIG-TIG Double-Sided Arc Welding of Copper-Stainless Steel Using Different Filler Metals, *J. Mater. Process.*, 2020, **55**, p 208–219

24. J. Luo, J. Xiang, D. Liu, F. Li, and K. Xue, Radial Friction Welding Interface Between Brass and High Carbon Steel, *J. Mater. Process. Technol.*, 2012, **212**, p 385–392

25. J. Kar, S.K. Roy, and G.G. Roy, Effect of Beam Oscillation on Electron Beam Welding of Copper with AISI-304 Stainless Steel, *J. Mater. Process. Technol.*, 2016, **233**, p 174–185

26. Y. Meng, X. Li, M. Gao, and X. Zeng, Microstructures and Mechanical Properties of Laser-Arc Hybrid Welded Dissimilar Pure Copper to Stainless Steel, *Opt. Laser Technol.*, 2019, **111**, p 140–145

27. H. Yang, G. Jing, P. Gao, Z. Wang, and X. Li, Effects of Circular Beam Oscillation Technique on Formability and Solidification Behaviour of Selective Laser Melted Inconel 718: From Single Tracks to Cuboid Samples, *J. Mater. Sci. Technol.*, 2020, **51**, p 137–150

28. K. Bhansali, A.J. Keche, C.L. Gogte, and S. Chopra, Effect of Grain Size on Hall-Petch Relationship During Rolling Process of Reinforcement Bar, *Mater. Today Proc.* 2020, **26**, p 3173–3178

29. M. Yu, H. Zhao, F. Xu, T. Chen, L. Zhou, X. Song, and N. Ma, Influence of Ultrasonic Vibrations on the Microstructure and Mechanical Properties of Al/Ti Friction Stir Lap Welds, *J. Mater. Process. Technol.*, 2020, **282**, p 116676

Publisher's Note Springer Nature remains neutral with regard to jurisdictional claims in published maps and institutional affiliations.